J. Fluid Mech. (2025), *vol.* 1010, A34, doi:10.1017/jfm.2025.321

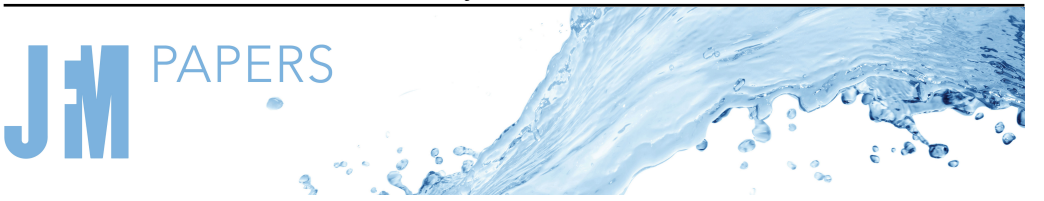

The settling of perforated disks in quiescent and turbulent air

Amy Tinklenberg[1,2], **Michele Guala**[1,3] **and Filippo Coletti**[4]

[1]Saint Anthony Falls Laboratory, University of Minnesota, Minneapolis, MN 55414, USA

[2]Department of Aerospace Engineering and Mechanics, University of Minnesota, Minneapolis, MN 55455, USA

[3]Department of Civil Environmental and Geo- Engineering, University of Minnesota, Minneapolis, MN 55455, USA

[4]Department of Mechanical and Process Engineering, ETH Zürich, Zürich 8092, Switzerland

Corresponding authors: Michele Guala, mguala@umn.edu; Amy Tinklenberg, atinklenberg@gmail.com

(Received 9 December 2024; revised 18 March 2025; accepted 20 March 2025)

The settling velocity of frozen hydrometeors in the atmospheric surface layer depends on their inertial and drag properties, and on the intensity of ambient turbulence. Thin, solid and perforated circular disks have been investigated through high-speed imaging, under laboratory conditions, to reproduce the settling of snow plates and dendrites in quiescent and turbulent flows. Different perforations made it possible to test the parameterisation of the fall speed in quiescent air, based on the geometric description of the solidity of the disk cross-sectional area. Interestingly, different falling styles, ranging from stable horizontal to fluttering and tumbling, were observed to depend significantly on the perforation geometry, which resulted in the stabilisation of the particle rotation and in a modulation of the drag coefficient. Ambient turbulence is observed to primarily induce cross-flow drag on the disks settling in the nonlinear regime, causing a reduction of the settling velocity in all cases investigated. Turbulence also manifests a secondary effect on the disk rotational dynamics, in particular when tumbling and stable falling styles co-exist, based on the phase space defined by the Reynolds number Re and the inertia ratio I^*. The interaction between ambient turbulence, particle anisotropy and permeability and the likelihood of tumbling is inferred to be the main reason for the observed settling velocity variability of snow dendrites in nature.

Key words: atmospheric flows, homogeneous turbulence

1. Introduction

In the study of frozen hydrometeors, disk-like particles can be used to reproduce the settling dynamics of ice plates and dendrite crystals at laboratory scale (Willmarth *et al.* 1964; Locatelli & Hobbs 1974; Kajikawa 1992; Garrett & Yuter 2014; Li *et al.* 2023; Singh *et al.* 2023; Li *et al.* 2024; Tinklenberg *et al.* 2023, 2024). The terminal velocity of hydrometeors is reached when the drag and the weight forces acting on the particles are balanced. The drag force on disk-like settling particles is defined by $F_d = (1/2)\rho C_D A_s V_t^2$, based on the terminal velocity V_t, the fluid density ρ, the projected solid drag area A_s (determined by its orientation with respect to the vertical direction coincident with the settling velocity) and the drag coefficient C_D. The latter accounts for the viscous shear stress between the fluid and the particle, which dominates at low Reynolds number $Re = V_t D/\nu$, (where ν is the kinematic viscosity) and the pressure gradient established between the leading and trailing surfaces of the particle, which represents a form drag contribution. This depends on the particle orientation and wake, and thus on Re. In the study of the drag of disk-like or nearly spherical frozen hydrometeors, such as plates or graupels, it is typically assumed that the nominal frontal area for a particle of diameter D is $A = \pi D^2/4$. However, this is not always a correct assumption. When assuming a nominal frontal area, C_D should include effects of preferential orientation of settling hydrometeors and unsteadiness due to fluttering and/or tumbling motions, both contributing to temporal fluctuations of the frontal area. This implies a strong coupling between the snow's rotational and translational dynamics, especially for anisotropic particles that tend to be rotationally unstable. In the limit of a thin disk, the diameter to thickness aspect ratio $\chi = D/h$ and the solid-to-fluid density ratio $\tilde{\rho} = \rho_s/\rho$, are the two parameters controlling the inertia ratio $I^* = (\pi/64)\tilde{\rho}/\chi$. Here, I^* represents the moment of inertia of the disk normalised by a term ρD^5, proportional to the moment of inertial of a circumscribed sphere of surrounding fluid (Willmarth *et al.* 1964); I^* plays a key role in the falling style and rotational dynamics of a settling disk. In particular, in the non-Stokesian, fully nonlinear drag regime relevant to frozen hydrometeors, that often settle at the terminal velocity V_t. This leads to $Re > 100$ (Tinklenberg *et al.* 2023), under which the Jefferey solution for the viscous torque does not apply (Jeffery 1922). The stabilising effect induced by increasing rotational inertia, I^*, has been correlated with the decrease of the rotational Strouhal number, $Str = fD/V_t$, which is a dimensionless form of the disk tumbling frequency, f, and is proportional to the tip speed ratio of the rotating disk (Willmarth *et al.* 1964; Auguste *et al.* 2013; Tinklenberg *et al.* 2023).On the other hand, inertia can also trigger oscillatory motions in falling particles. Frozen hydrometeors are usually associated with values of I^* orders of magnitude larger than in typical laboratory experiments in water, due to the much higher solid-to-fluid density ratio (Stout *et al.* 2024). This has been indicated as the cause of oscillations of non-spherical particles falling in air at Re as low as 5 (Bhowmick *et al.* 2024), which contrasts with observations in water.

When approaching realistic snow morphologies during natural snowfall, an additional complication must be accounted for. Due to riming, the snow crystal morphology can vary widely not only in the overall shape of the drag area, but also in how the internal structure evolves. This affects the particle density and porosity (Locatelli & Hobbs 1974; Garrett & Yuter 2014; Li *et al.* 2023). The presence of pores (and in general openings) within the hydrometeor structure allows the flow to penetrate it during its descent. This permeability has not been directly considered in studies of frozen hydrometeors, but was systematically investigated in recent studies of rising and falling thin plates, indicating a profound influence on the falling style (Vagnoli *et al.* 2023; Sánchez-Rodríguez & Gallaire 2025).

Frozen hydrometeor density has been observed to widely vary depending on morphological types, wind, air temperature and humidity conditions, and still represents

an area of active research (Magono & Lee 1966; Locatelli & Hobbs 1974; Brandes *et al.* 2008; Li *et al.* 2023; Singh *et al.* 2023). Irregularities in the nominal area and solidity of snow plates and dendrites have been accounted by List & Schemenauer (1971) and Böhm (1989) in the formulation of a modified drag coefficient curve $C_D = f(Re,\ A_R)$, which incorporates the ratio A_R of the crystal cross-sectional solid area A_s to that of a circumscribed disk A. The Böhm (1989) drag model incorporates the development of shear layers from the particle edges, assuming a flat, horizontal falling style, i.e. with the largest nominal area exposed to the relative flow.

More recently, a variety of laboratory studies aimed to analyse the area ratio effect more systematically. Vincent *et al.* (2016) considered annular disks settling, i.e. disks with a singular centred hole, and compared their laboratory findings with solid equivalents. As the central hole size is increased, they find strengthening stabilisation due to the development of an additional counter-rotating vortex ring at the hole edge, which acts in opposition to the vortex ring shed at the outer edge. This was confirmed in the recent laboratory experiments of Zhang *et al.* (2023). The stabilising effect forces the tumbling behaviour of the corresponding solid disk to be dampened into a fluttering motion, in particular for $d_i/d_o \approx 0.3 \pm 0.1$, where d_i is the inner hole diameter and d_o is the outer diameter of the disk, corresponding to an area ratio of $\simeq 0.9$. Even if the single hole shape is not representative of dendrites, the physical connection between disk permeability and rotational stability is of interest. Westbrook & Sephton (2017) and McCorquodale & Westbrook (2021*a*) approach this problem with direct relevance to frozen hydrometeors through the use of 3D-printed analogues of complex ice particles. Their laboratory experiments confirm the robustness of the model proposed by Böhm (1989), and later modified by Heymsfield & Westbrook (2010), except in the case of very thin and flat particles. While these experiments were able to match the particle Reynolds number, the settling dynamics in liquids did not preserve I^*, thus limiting the range of falling styles and the coupled rotation–translation that frozen hydrometeors may experience in air (Kajikawa & Okuhara 1997). At the field scale, Auer & Veal (1970) and Vázquez-Martín *et al.* (2021) suggested that ice plates are among the shape groups with the lowest area ratios, and in turn exhibit reduced velocities, highlighting the importance of this parameter, along with particle anisotropy, in drag force predictive models. Li *et al.* (2024) measured the shape and density of natural snow particles and identified events with dominant morphological types: dendrites and plates were again observed to have a higher drag coefficient with respect to the Böhm (1989) model. Both results indicate that plates and dendrites experience higher drag than approximately round particles, such as graupel, with the same nominal diameter. This suggests that a flat preferential orientation characteristic of fluttering, as opposed to tumbling, is more likely to occur.

Measurements during natural snow fall defines the parameter space of interest, but faces another additional complication represented by the effect of ambient turbulence. Particle–turbulence interactions cover a range of ubiquitous and intricate mechanisms that depend on particle size, (an)isotropy, inertial properties and on the ambient turbulent scales (Voth & Soldati 2017; Brandt & Coletti 2022). Preferential sweeping induces high velocity paths along the downward side of vortical motions where (usually spherical sub-Kolmogorov) particles tend to settle faster than in quiescent flows (Wang & Maxey 1993; Aliseda *et al.* 2002; Garrett *et al.* 2012; Ferrante & Elghobashi 2003; Li *et al.* 2021*b*). Loitering, cross-flow-induced drag or other nonlinear drag effects drive particles along convoluted or high flow resistance paths, reducing their average settling velocity (Singh *et al.* 2023; Bagheri & Bonadonna 2016; Tinklenberg *et al.* 2024). In addition, particle rotational instabilities, governing the statistical occurrence of tumbling and fluttering, were observed to be amplified by the fluctuating velocities of ambient turbulent flows, even if the tumbling

frequency was primarily controlled by the disk inertial properties I^* (Tinklenberg *et al.* 2024). Both preferential orientation and the particle angular velocity are inferred to modulate the particle wake and the drag coefficient. Therefore, experimental studies of plate crystals and dendrites settling in a laboratory set-up should include (i) a large number of realisations in ambient turbulence, so that the cumulative effect of different falling styles can be statistically captured in the settling velocity ensemble averages, and (ii) a similarly large sample in quiescent flow, so that the effect of turbulence can be disentangled from the variability of falling styles and orientations.

We call attention to the lack of studies of complex particle geometries performed in air turbulence. Besides field data collected in the atmospheric surface layer, there is little focus on realistic particle geometries, including permeability and anisotropic features as both area and aspect ratios, and the interaction with ambient turbulence and wind of varying intensity. This is particularly relevant for the prediction of the terminal velocities of snow plates and dendrites in atmospheric turbulence, which present the challenges of being thin, perforated and prone to tumbling. In our current laboratory study, we control the disk material properties and geometries, thus limiting the uncertainty associated with the particle density, size and weight, which are challenging to measure during natural snowfalls, along with their direct effect on the terminal velocity. Our set-up allows us to explore particles with size, density and fall speed comparable to differently rimed snow dendrites and plates (Locatelli & Hobbs 1974) in turbulent air flows comparable to low–moderate wind conditions during snowfalls in the atmospheric surface layer (Nemes *et al.* 2017; Li *et al.* 2024). The main questions we address in this work are on the stabilising effect of disk perforations under quiescent and ambient turbulent flows, and on the relevance of the area ratio in the prediction of the particle drag and terminal velocity. We eventually hope to shed some light on the coupling between tumbling and falling motions for solid and perforated disks, and better assess the snow particle drag modelling approach proposed by Böhm (1989) and Heymsfield & Westbrook (2010) under well controlled laboratory conditions.

In our *ad hoc* designed laboratory facility, we cover the relevant region in the $I^* - Re$ parameter space (Kajikawa & Okuhara 1997) and generate root mean square (r.m.s.) velocity fluctuations u' consistent with atmospheric flows, reaching a Reynolds number $Re_\lambda = u'\lambda/\nu \simeq 400$, where λ is the Taylor micro-scale (Carter *et al.* 2016). We vary the disk thickness, area ratios and perforation geometry, and quantify their effect on the fall speed, drag coefficient and rotational kinematics, extending the dimensionless parameter space investigated by Tinklenberg *et al.* (2023, 2024).

The paper is organised as follows. In the following section (§ 2) we describe the disk inertial properties along with snow plate and dendrite drag models, and we provide an overview of the experimental set-up. Section 3 is devoted to the experimental results on the disk translational dynamics (average settling velocity, drag coefficient and trajectory angle) and rotational dynamics (orientation and tumbling) in quiescent and turbulent conditions. Our experimental observations are compared with field-scale results in the discussion (§ 4). Conclusions follow.

2. Methodology

2.1. *Disk properties and fabrication*

The particles utilised in the laboratory experiments are thin disks of both solid and perforated geometries. Figure 1(*a*) shows images of every disk type considered. All of the solid disks are made of polyethylene terephthalate (PET), with a density of

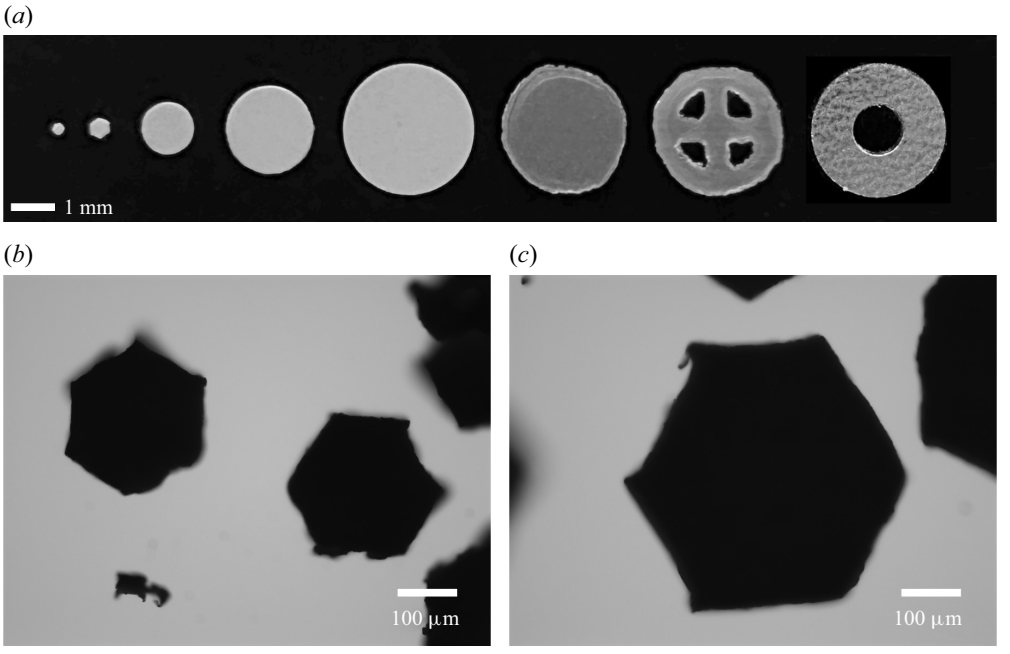

Figure 1. Images of all disks studied. (*a*) From left to right, D increasing from 0.3 to 3 mm°. (*b*) Microscope images of 0.3 mm and of (*c*) 0.5 mm disks.

$\rho_d = 1380\ \mathrm{kg\,m^{-3}}$. Disks with nominal diameters of 0.3 mm, 0.5 mm, 1 mm, 2 mm and 3 mm (as referenced in table 1) are manufactured for use as commercial glitter, all with a thickness of $h = 50\ \mu\mathrm{m}$. Their settling dynamics is described in Tinklenberg *et al.* (2024). Thicker disks of $h \approx 100\ \mu\mathrm{m}$, are manufactured with a commercial laser cutter out of PET sheets. Two classes of such disks are produced: a solid geometry shown in figure 2(*a*) and a four-quadrant, perforated geometry shown in figure 2(*b*). Both are approximately 3 mm in diameter; we refer to them as 3 mm* and 3 mm$^{\times}$, respectively. The single hole (3 mm°) disks were selected to match the open area of the four quadrant (3 mm$^{\times}$) disks. The laser cutting method which produced the 3 mm$^{\times}$ did not warrant sufficient precision in the case of the 3 mm°, in particular with respect to the centre location of the single hole. The 3 mm° were thus commercially manufactured as sequins, with a measured density of 2454 kg m^{-3}, and chosen for the similar diameter and open area ratio of the 3 mm$^{\times}$.

Dimensions of a subset of 30 disks per diameter are directly measured and yield the mean and standard deviations listed in table 1, along with the key physical parameters for each disk type. The diameters are obtained by imaging disks lying on a tray, while the thicknesses are obtained by tightening calliper teeth on stacks of various numbers of disks and calculating the average thickness in each stack, confirming the specification from the vendor. The 0.3 mm and 0.5 mm disks are hexagonal in shape (see figure 1(*b*, *c*)) and we take D as the diameter of the circumscribing circle, as is common in the hydrometeor literature (Böhm 1989; Heymsfield & Westbrook 2010).

The area ratio is defined as $A_R = A_s/A$, where A_s is the actual solid area of each disk geometry and $A = \pi D^2/4$ is the solid disk area of the minimum circumscribing circle of A_s (see figure 3). As the disk orientation is unknown and often rapidly varying during tumbling or fluttering motions, we consider all projected areas always corresponding to the maximum drag area of a flat (or horizontal) falling disk. For the sake of notation clarity, we recall that the solid area A_s is defined as A_e in Böhm (1989) and as A in Heymsfield &

Nominal diameter	D [mm]	h [mu m]	χ	$\tilde{\rho}$	A_R	U_g [m s^{-1}]	Ga	I^*	$Sv_L(w)$	$Sv_L(s)$
0.3 mm	0.28 ± 0.01	50.0 ± 7.5	5.5	1150	1	1.06	14.0	14.11	1.14	0.76
0.5 mm	0.50 ± 0.02	50.0 ± 7.5	10.0	1150	1	1.06	28.1	7.06	2.14	1.43
1 mm	1.27 ± 0.07	50.0 ± 7.5	25.4	1150	1	1.06	89.4	2.22	2.29	1.43
2 mm	2.02 ± 0.03	50.0 ± 7.5	40.4	1150	1	1.06	142.2	1.40	2.46	1.64
3 mm	3.03 ± 0.02	50.0 ± 7.5	60.6	1150	1	1.06	213.3	0.93	3.59	2.39
3 mm*	2.80 ± 0.07	101.6 ± 5.1	28.3	1150	1	1.51	234.1	2.06	4.62	3.08
3 mm$^\times$	3.03 ± 0.05	101.6 ± 5.1	29.8	1150	0.73 ± 0.06	1.51	253.4	1.57	4.56	3.04
3 mm°	3.17 ± 0.01	110.0 ± 6.4	28.8	2045	0.76 ± 0.03	2.10	367.8	2.84	6.32	4.21

Table 1. Disk properties including the measured mean disk diameter D, the measured mean disk thickness h, both listed with $\pm$ one standard deviation (σ). Also included are the diameter to thickness aspect ratio $\chi = D/h$, the density ratio $\tilde{\rho} = \rho_d/\rho_f$, the disk area ratio $A_R = A_s/A$, the Galileo number $Ga = U_g D/\nu$, where $U_g = \{2|\tilde{\rho} - 1|gh\}^{1/2}$ is the gravitational velocity, and the inertia ratio $I^* = (\pi/64)\tilde{\rho}/\chi$. To calculate I^* of the perforated disk, we use the geometry on which the laser-cutter manufacturing is based. The settling velocity number, $Sv_L = V_{t,0}/u'$, is listed for the both turbulence conditions tested as $Sv_L(w)$ and $Sv_L(s)$, referring to weaker and stronger turbulence, respectively (see table 2 for the flow statistics).

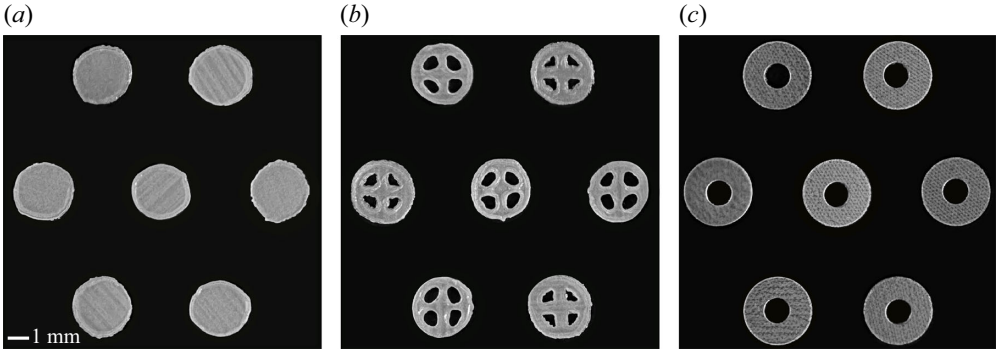

Figure 2. Image groupings of laser cut and perforated disks showing the variation within the populations of the (*a*) 3 mm*, (*b*) 3 mm$^\times$ and (*c*) 3 mm°.

Westbrook (2010). Here, A_R is measured for a subset of 100 disks for 3 mm*, 3 mm$^\times$ and 3 mm° by imaging the individual disks with a calibration length in the frame. Binarisation of the image allows the solid disk pixels to be identified and compared with the area of the minimum encompassing circle of each. These values are also summarised in table 1. Note that $A_R = 1$ for all the solid disk types. Disk geometric and kinematic variables, along with a basic schematics of the experimental apparatus and reference system, are illustrated in figure 3.

2.2. *Disk kinematics phase space*

The pioneering laboratory work of Willmarth, Hawk & Harvey (1964) established the use of the inertia ratio $I^* = I/(\rho_f D^5)$, normalising the disk moment of inertia I (around the central axis parallel to its diameter) with a scaling quantity $\rho_f D^5$ proportional to the moment of inertia of a surrounding fluid sphere. This formula is used to calculate the inertia ratio for the perforated geometries. For a solid thin disk of thickness h, the inertia is derived as $I^* = (\pi/64)\tilde{\rho}/\chi$, with the aspect ratio $\chi = D/h$ assumed much larger than unity (Field *et al.* 1997; Auguste, Magnaudet & Fabre 2013; Lau, Huang & Xu 2018).

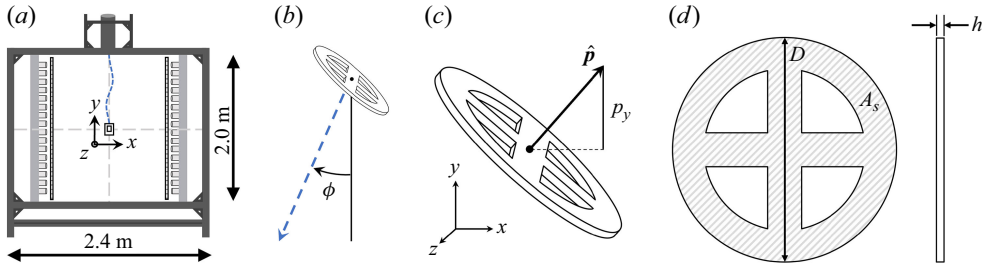

Figure 3. (*a*) Turbulence facility diagram including global coordinate system and basic dimensions. (*b*) Definition of the disk trajectory angle ϕ. (*c*) Representation of the disk orientation vector $\hat{\boldsymbol{p}}$ and its vertical component p_y. (*d*) Definition of the disk solid area A_s, nominal diameter D, and thickness h.

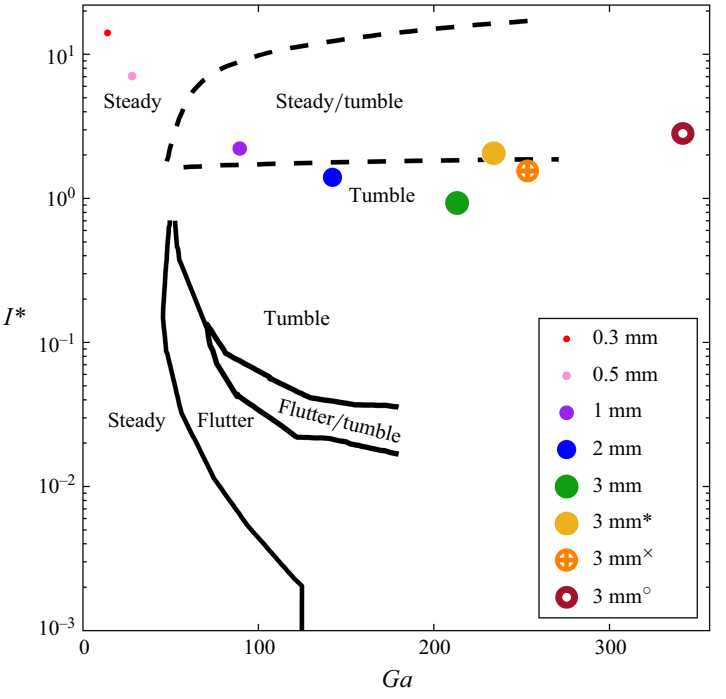

Figure 4. Falling style parameter space of I^* versus Ga with disks in the current study placed among data from the literature. Solid black lines show the falling mode boundaries identified by Auguste *et al.* (2013). Dashed black lines indicate upper and lower boundaries of the region of bistability found by Lau *et al.* (2018).

The parameter I^* has been used to predict the different falling styles in a parameter space along with the Galileo number $Ga = U_g D/\nu$ (Chrust, Bouchet & Dušek 2013; Moriche, Uhlmann & Dušek 2021; Moriche *et al.* 2023; Tinklenberg *et al.* 2023). The convenience of using Ga rather than Re stems from the *a priori* definition of the gravitational velocity $U_g = \{2|\tilde{\rho} - 1|gh\}^{1/2}$ (where g is the gravitational acceleration) which is a reasonable approximation of V_t if the drag coefficient C_D is of order unity (and Re independent). Figure 4 depicts the $I^* - Ga$ regime map based on several of the above mentioned studies, with values summarised in table 1. Also indicated are the cases considered in the present paper, which are designed to be representative of plate crystals falling in the atmosphere. However, Vincent *et al.* (2016) noted that the falling mode transitions of solid disks do not predict the behaviour transitions of perforated geometry disks.

Forcing	u_η $[m\,s^{-1}]$	η $[mm]$	τ_η $[ms]$	λ $[mm]$	u' $[\mathrm{m\,s^{-1}}]$	L $[cm]$	T_L $[s]$	ε $[m^2\,s^{-3}]$	Re_λ $[-]$	Re_L $[-]$	LSA $[-]$
Weaker	0.056	0.28	4.9	9.6	0.50	10.0	0.20	0.6	311	3200	1.69
Stronger	0.068	0.24	3.7	10.3	0.75	12.8	0.16	1.1	473	6400	1.67

Table 2. Turbulent flow statistics for the forcing conditions investigated. Kolmogorov scales of velocity u_η, length η and time τ_η; Taylor microscale λ; integral scales of (r.m.s.) velocity u', length L and time τ_L; dissipation ε; and Reynolds numbers $Re_\lambda = u'\lambda/\nu$ and $Re_L = u'L/\nu$. Weaker turbulence corresponds to G6 forcing, with grids in place to diffuse the jets, while stronger turbulence corresponds to B6 forcing, as described in Carter *et al.* (2016).

2.3. *Experimental apparatus and turbulence properties*

Turbulence is generated via two vertical panels facing each other at 1.81 m apart in an enclosed chamber. Each panel has 128 nozzles distributed in a planar array of 8 x 16 (see figure 3*a*). All the nozzles are connected to a pressurised air line at 700 kPa and attached to computer-controlled solenoid valves. These are actuated independently to induce each jet in a randomised sequence following the sun-bathing algorithm proposed by Variano & Cowen (2008). A region of approximately homogeneous turbulence with negligible mean flow is formed in the central section of the facility of size $O(1\ \mathrm{m}^3)$. The intensity of the turbulence fluctuations is varied by controlling the mean actuation time of the jets, and reduced by adding square-mesh grids in front of the jet arrays. The random-jet forcing is run for sufficient time to allow the homogeneous region of turbulence to reach a statistically stationary state and is sustained throughout the duration of each experiment. The flow characterisation of the facility is described in detail in Carter *et al.* (2016) and Carter & Coletti (2017, 2018). It has been used extensively to study particle turbulence interaction for the cases of small spherical particles (Petersen *et al.* 2019; Berk & Coletti 2021; Hassaini & Coletti 2022; Hassaini *et al.* 2023) and for the settling of solid disks in quiescent and turbulent flows (Tinklenberg *et al.* 2023, 2024).

We operated the turbulent chamber with and without the square-mesh grids, corresponding to the nominal definitions of 'weaker turbulence' and 'stronger turbulence', as summarised in table 2, and consistent with the solid disk experiments by Tinklenberg *et al.* (2024). The dissipation rate ε is higher than typical levels in clouds (Grabowski & Wang 2013), but η is comparable to that encountered in the atmospheric surface layer through which hydrometeors precipitate (see, e.g. the field studies by Li *et al.* 2021*a*, where $\eta \sim 0.5$ mm, or values of $\eta = O(1\ \mathrm{mm})$ reported by Nemes *et al.* 2017 and Shaw 2003). The r.m.s. velocity fluctuations u' yield realistic values of the settling velocity number Sv_L (see, e.g. Nemes *et al.* 2017 and Li *et al.* 2021*a*, where $Sv_L = 0.60 - 10.7$), which is expected to be influential for the settling dynamics (Wang & Maxey 1993; Good *et al.* 2014; Byron *et al.* 2015; Fornari *et al.* 2016*a*,*b*; Petersen *et al.* 2019; Brandt & Coletti 2022).

2.4. *Experimental methods and disk image analysis*

The facility operation, imaging techniques and post-processing methods were described in Petersen *et al.* (2019) and Tinklenberg *et al.* (2023, 2024). Those are briefly summarised here. With the homogeneous region of turbulence in a statistically stationary state, a sieve shaker positioned above the 3 m long chute leading into the chamber releases disks at a chosen volume fraction of $\Phi_V = O(10^{-5})$. The disks fall for approximately 1 m inside the chamber before reaching the camera field of view.

The imaging plane is positioned vertically in the centre of the chamber, illuminated by a 3 mm thick laser sheet. Images are captured via a high-speed CMOS camera (Phantom VEO 640) operated at 4300 Hz. A 105 mm Nikon lens collects images at 11.4 pixels mm^{-1} in a 11.2 cm $\times$ 8.4 cm field of view. To account for any run-to-run variability and increase statistical convergence, five experimental runs each lasting approximately 10 s are performed at minimum for each disk type and flow condition. This number of runs captures statistics of $O(10^3 - 10^4)$ individual disk trajectories for each case, with typical trajectory lengths of $O(10^2)$ frames.

Binarising the images allows for the disks to be identified and filtered based on their intensity, size and sharpness. The image intensity gradient obtained by Sobel approximation identifies blurry objects to be removed. Disks are individually fit with an ellipse, resulting in sub-pixel-accurate centroid location and major axis orientation. The ellipse fits are used to reconstruct disk orientations in three dimensions. An orientation vector, $\hat{\boldsymbol{p}}$, along the axis of rotational symmetry of the disk, can then be obtained following Baker & Coletti (2022). Finally, the centroid trajectories and orientation progressions are convolved with a Gaussian kernel in time to reach the smoothed translational and rotational disk motions.

2.5. *Thin disk drag models*

A semi-empirical formula has been proposed by Böhm (1989) and Heymsfield & Westbrook (2010), among others, to predict the settling velocity of frozen hydrometeors. The model is inspired by the early work of Abraham (1970) on the drag of a spherical particle based on an inviscid term C_0 and a Re-dependent contribution representing the boundary layer developing from the edge of the sphere, namely $C_D^{sph} = C_0(1 + (\delta_0/Re^{1/2}))^2$, where δ_0 is a fitting constant.

Böhm (1989) and Heymsfield & Westbrook (2010) extended the model of Abraham (1970) to generic snow particles, in fact assuming a master drag equation for frozen hydrometeors $C_{DM} = C_D^{sph}$ with a new set of fitting parameters. They introduced the Best, or Davies, number $X = C_{DM}Re^2$ to eliminate the settling velocity from the equation, imposing the equilibrium of drag and weight forces and only accounting for inertial and geometrical snow properties in the estimate of X (see step 1 in table 3). The area ratio A_R was introduced to include different snowflake geometries while maintaining the ability of the formulation and parameters of the master drag model C_{DM} to describe specific snow particle drag coefficients precisely as $C_D = A_R^{-n}C_{DM} = A_R^{-n}C_0(1 + (\delta_0/Re^{1/2}))^2$. Ongoing efforts are still devoted to fitting or altering the model parameters C_0, δ_0 and $n > 0$ to achieve a universal dependency of the area ratio for a variety of complex snow morphologies (needles, dendrites, stellars and aggregates) and to collapse all the re-scaled, particle-specific drag coefficients on the master curve (McCorquodale & Westbrook 2021*a*, *b*). With all disk properties measured, the step 1 equation in table 3 can be inverted to obtain the settling Reynolds number (step 2), and eventually the settling velocity V_t (step 3). Note that Böhm (1989) and Heymsfield & Westbrook (2010) use different coefficients C_0 and δ_0 and a different power-law exponent $n = 0.75 - 0.5$ to account for the area ratio, but share the same master drag equation. The differences in the formulation and in the fitting parameters are attributed primarily to different types of data sets considered in the validation, including snowflakes in air and artificial snow particles settling in liquids (see also Böhm 1992; Mitchell 1996; Khvorostyanov & Curry 2002, 2005; Mitchell & Heymsfield 2005, among many others).

It is, however, important to stress that the effect of air turbulence has never been explicitly included – in terms of loitering, cross-flow-induced drag, preferential sweeping

Step 1	$X = C_{DM} Re^2 = (\rho_f/\mu^2)(8mg/\pi A_R^{1-n})$	Parameters
Step 2	$Re = (\delta_0^2/4)[(1 + ((4\sqrt{X})/(\delta_0^2\sqrt{C_0})^{1/2})) - 1]^2$	Böhm (1989) $C_0 = 0.6$, $\delta_0 = 5.83$ and $n = 3/4$
Step 3	$V_t = \mu Re/\rho_f D$	Heymsfield & Westbrook (2010) $C_0 = 0.35$, $\delta_0 = 8.0$, $n = 1/2$

Table 3. Step by step procedure for the estimate of the terminal velocity V_t of a solid or perforated disk, given μ, ρ_f, m, A_R and D, as originally proposed by Böhm (1989). The parameters C_0 and δ_0 are defined in the master drag equation $C_{DM} = C_0(1 + (\delta_0/Re^{1/2}))^2$. Updated C_0, δ_0 coefficients and area ratio power-law dependency A_R^{1-n} provided by Heymsfield & Westbrook (2010) are listed for comparison.

Method	0.3 mm [m s^{-1}]	0.5 mm [m s^{-1}]	1 mm [m s^{-1}]	2 mm [m s^{-1}]	3 mm [m s^{-1}]	3 mm* [m s^{-1}]	3 mm$^{\times}$ [m s^{-1}]	3 mm$^{\circ}$ [m s^{-1}]
Quiescent V_t	0.57 ± 0.06	1.07 ± 0.12	1.14 ± 0.17	1.23 ± 0.31	1.79 ± 0.44	2.31 ± 0.47	2.28 ± 0.25	3.16 ± 0.33
Böhm (1989)	0.46 (−19.9 %)	0.59 (−44.7 %)	0.80 (−29.6 %)	0.89 (−27.3 %)	0.97 (−46.0 %)	1.44 (−37.5 %)	1.26 (−44.6 %)	1.75 (−44.4 %)
Mitchell (1996)	0.46 (−19.9 %)	0.59 (−44.7 %)	0.80 (−29.6 %)	0.89 (−27.3 %)	0.97 (−46.0 %)	1.44 (−37.5 %)	1.52 (−33.1 %)	2.03 (−35.6 %)
Heymsfield & Westbrook (2010)	0.49 (−13.6 %)	0.66 (−38.0 %)	0.95 (−16.9 %)	1.08 (−12.4 %)	1.18 (−34.0 %)	1.88 (−18.4 %)	1.90 (−16.7 %)	2.87 (−9.1 %)

Table 4. Empirically derived velocity estimation method results from Böhm (1989), Mitchell (1996) and Heymsfield & Westbrook (2010). The terminal velocities are listed with ± one standard deviation. Errors shown in parentheses below each velocity estimate are computed in comparison with the measured V_t in quiescent air in the current study.

or induced variability in falling styles. Therefore, the resulting V_t estimates from all formulations summarised in table 3 are generally associated with quiescent flow conditions (Nemes *et al.* 2017; Li *et al.* 2021*b*; Singh *et al.* 2023; Li *et al.* 2024). Our apparatus provides the opportunity to compare these models under controlled quiescent and turbulent flow conditions, reasonably consistent density ratios and without the uncertainties in particle size and mass associated with natural snowfalls.

3. Results

3.1. *Mean settling velocity and drag coefficient*

We first apply the models of Böhm (1989) and Heymsfield & Westbrook (2010) to the current disks and compare with the velocities measured in quiescent air. Summarised in table 4, we find that applying the model and coefficients of Böhm (1989) using the area ratio for each disk geometry yields an average error compared with the measured velocities of −36.7 % (the model underestimates the measured velocities in quiescent conditions). If we use the same C_0 and δ_0 coefficients estimated by Böhm (1989) but ignore the area ratio of the perforated disks, thus treating them as solid disks ($A_s = A$), we are in fact adopting the approach by Mitchell (1996), still leading to a significant -34.2 % underestimation of the settling velocity. The adjusted coefficients and dependency on the area ratio of Heymsfield & Westbrook (2010) improves the average estimated velocity error to -19.9 %.

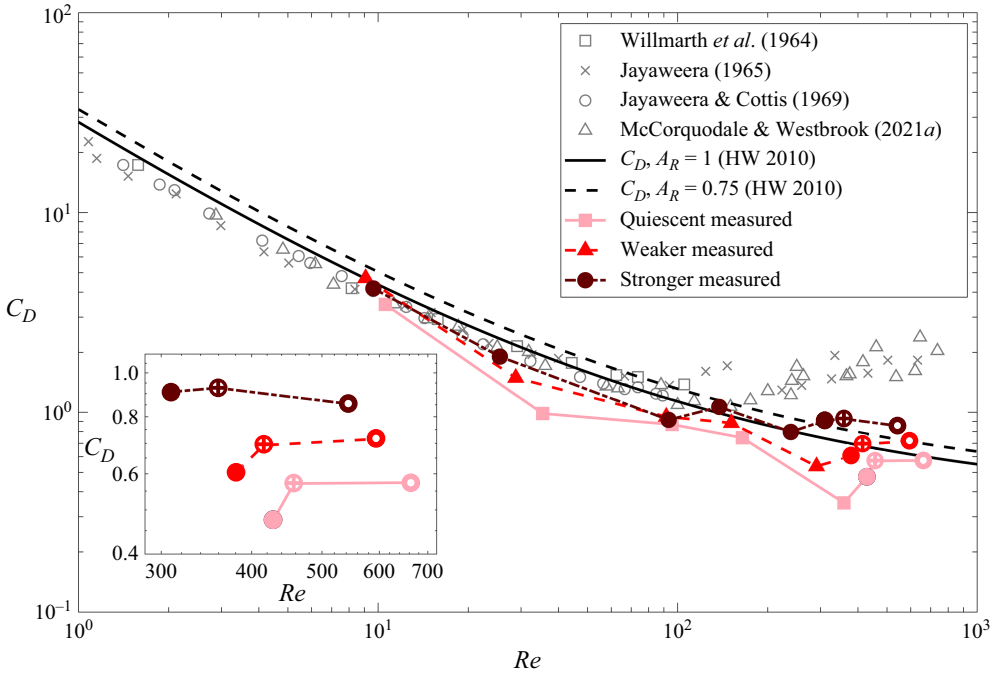

Figure 5. Drag coefficient versus Reynolds number curves plotted from measurements in quiescent air, weaker turbulence and stronger turbulence. Data included in grey symbols from Willmarth *et al.* (1964), Jayaweera & Mason (1965), Jayaweera & Cottis (1969) and McCorquodale & Westbrook (2021*a*). The empirically derived drag curve from Heymsfield & Westbrook (2010) is shown by the solid black line and the dashed black line is re-scaled for the area ratio of our perforated disks. The inset focuses on an axis range around the data points from the perforated disk measurements. Data from other publications digitised using WebPlotDigitizer (Rohatgi 2021).

The latter model seems to better capture the drag of larger disks falling at higher Re and the effect of permeability for the perforated disk geometries.

The disk drag coefficients $C_D = 2mg/\rho_f A_s V_t^2$ were estimated from the projected, solid disk area A_s assuming flat falling and the averaged measured settling velocity V_t. The latter is defined as the average of the vertical component of the particle velocity. The area ratio has a unitary value $A_R = 1$ for the solid disks, whose drag coefficient can be directly compared with the master drag curve, but the perforated geometries require rescaling. To compare the experimental results and the theoretical predictions, we plot the particle-specific drag coefficients C_D as the function of Reynolds number in figure 5, and scale the predictive curve(s) from the master equation. Inset in figure 5 is a zoomed in view on the perforated disks. The grey symbols are from low-density-ratio laboratory studies of disks, summarised by McCorquodale & Westbrook (2021*a*). The solid black curve following Heymsfield & Westbrook (2010) for the solid disks is given by $C_D = C_{DM} = C_0(1 + (\delta_0/Re^{1/2}))^2$. The dashed curve is the re-scaled prediction for perforated geometries ($C_D = C_{DM} A_R^{-1/2}$) using the power-law dependency of the area ratio proposed by Heymsfield & Westbrook (2010), which best reproduced the average settling velocity.

Our disk data, including those of the 3 mm$^{\times}$ and 3 mm$^{\circ}$ perforated geometries, align quite well with Heymsfield & Westbrook (2010). At low Re, non-tumbling solid disks are well captured by the master curve. With increasing Re and emerging variability in the

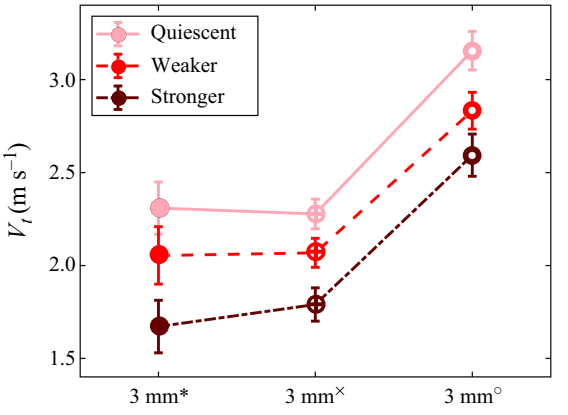

Figure 6. Mean vertical velocity V_t plotted by disk geometry in each flow condition.

disk falling styles, deviations are observed. Overestimated drag coefficients are associated with the above underestimated settling velocities. There are two possible reasons for this: (i) the orientation of a disk in our analysis is assumed flat in the definition of the projected drag area A_s, implying that any change in orientation, e.g. due to fluttering, contributes to reducing the drag force and increasing the settling velocity; (ii) when tumbling occurs, depending on both Re and I^*, the near wake, form drag and C_D are affected, generally resulting in a decrease in drag, as seen, e.g. when comparing the drag of a flat disk ($C_D \sim 1$) with the one of a sphere ($C_D \sim 0.5$) resembling a tumbling disk along with a tumbling mass of entrapped fluid. This follows what was found in the quiescent experiments of Tinklenberg *et al.* (2023): low-density-ratio experiments, even when matching Re of frozen hydrometeors in the atmosphere, may be slightly biased towards stable flat falling due to relatively lower I^* values. Rotationally unstable disks in air flows are expected to exhibit a more random orientation and a reduced drag area, on average, resulting in a higher settling velocity, as observed here. This difference is especially apparent starting at $Re \approx 100$ in figure 5, above which unsteady wakes, fluttering and tumbling are much more likely to occur, in particular for the higher-density-ratio cases (Willmarth *et al.* 1964; List & Schemenauer 1971; Bréon & Dubrulle 2004; Noel & Chepfer 2004). We thus infer that the more chaotic falling styles affecting frozen hydrometeors in the atmosphere must be incorporated into the calibration of predictive models. The model by Heymsfield & Westbrook (2010) incorporates both laboratory and field data of rimed and unrimed plates and dendrites into the calibration, which can be assumed to include some ambient turbulence, in addition to various falling styles. The formulation of Böhm (1989) compares with previous models and measurements from Locatelli & Hobbs (1974) for aggregates, but seems to include only laboratory data in a liquid tank, hence at low density ratio, for plate crystals up to $Re = 100$. The above differences may partially explain the better agreement between measured and predicted settling velocities using the Heymsfield & Westbrook (2010) model for quiescent flow conditions.

3.2. *Phenomenology of perforated versus solid disk settling in turbulent flows*

Figure 6 shows the mean vertical velocity plotted by disk geometry and forcing condition. Both the solid disks (3 mm*) and perforated disks (3 mm× and 3 mm°) experience a velocity reduction on average due to ambient turbulence. This was also observed for smaller diameter disks compiled in Tinklenberg *et al.* (2024). The higher settling velocity

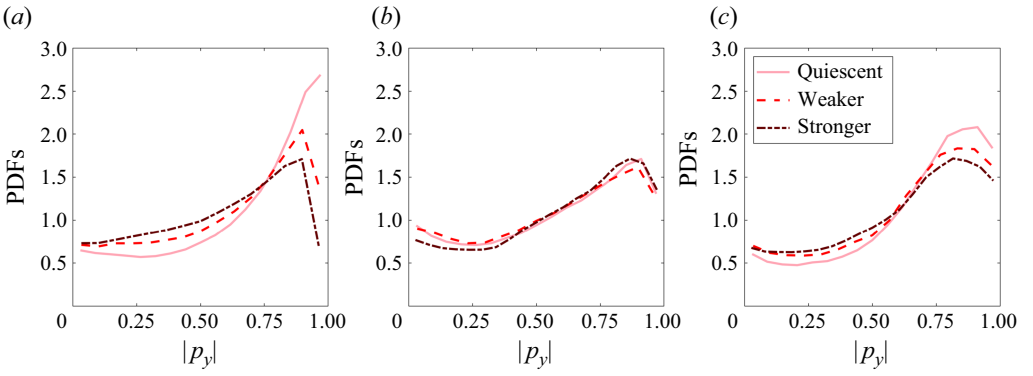

Figure 7. The PDFs of the modulus of the instantaneous disk orientation vector with respect to the vertical, $|p_y|$. Plotted at each forcing level for the (*a*) 3 mm*, (*b*) 3 mm$^{\times}$ and (*c*) 3 mm° disks. Here, $|p_y| \sim 0$ indicates an edge-on orientation and $|p_y| \sim 1$ indicates a flat-falling orientation.

observed for the 3mm° disk is primarily due to the increased material density, as predicted by all models in table 4. Particle settling variability is illustrated in the form of error bars and quantified by the standard deviation of all instantaneous points from all experimental runs, divided by the number of experimental runs. This method yields marginally smaller errors for both of the perforated geometries as compared with the solid particle, indicating that the perforated disks experience less variability in vertical velocity, in particular in quiescent flow. As discussed in Tinklenberg *et al.* (2024), the observed fluctuation of settling velocity results from the spatio-temporal variability of the disk orientations and the associated drag and wake. Thus, we infer that such a reduced variability could be associated with a more consistent falling dynamics.

Falling style, including preferential orientation and tumbling, has been shown to greatly influence the drag on plates at high density ratios (McCorquodale & Westbrook 2021*b*; Tinklenberg *et al.* 2023) and may explain the reduced variability in vertical velocity. In particular, the transition from tumbling to fluttering, discussed in Vincent *et al.* (2016) for the single hole coin, is inferred to increase the disk rotational stability and decrease the variability in orientation of our perforated disks.

Evidence of the effect of disk permeability and turbulence on preferential settling orientation is shown in figure 7, with the probability density functions PDFs of instantaneous $|p_y|$ (see figure 3*c* for the local orientation-dependent reference system). Plate geometries, if rotationally stable, are expected to settle predominantly with their maximum frontal area perpendicular to the fall speed direction ($p_y = 1$) in the limit of an infinitely thin disk – a limit which may not hold in the current scenario (Willmarth *et al.* 1964; Sassen 1980; Matrosov *et al.* 2001; Chrust *et al.* 2013; Wang 2021). This is observed in all experiments, in particular for the solid disk under quiescent conditions.

Increasing turbulence intensity tends to homogenise the orientation of disks that are prone to tumbling: the high-probability peak associated with steady falling of the solid disks in quiescent air is less pronounced, and resembles the distributions of perforated geometries with a broader hump ($0.75 < p_y < 1$), pointing at increased fluttering. The lesser variation in the perforated trends between the different turbulent conditions indicates that turbulence does not significantly change the orientation of perforated disks. This suggests that the observed appreciable variation in drag coefficients is due to the disks' rotational dynamics and their horizontal slip velocity, rather than to their variability in the projected area.

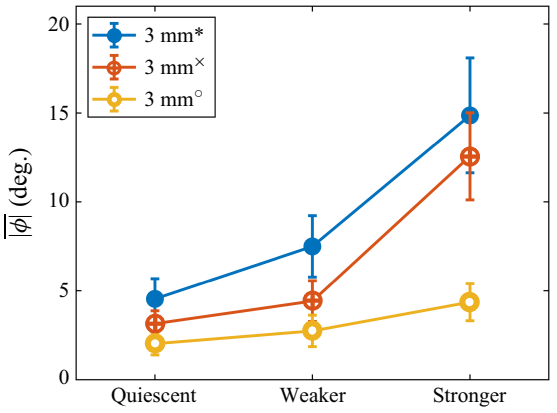

Figure 8. Average two-dimensional projected trajectory angles plotted for each forcing case with lines for each disk type.

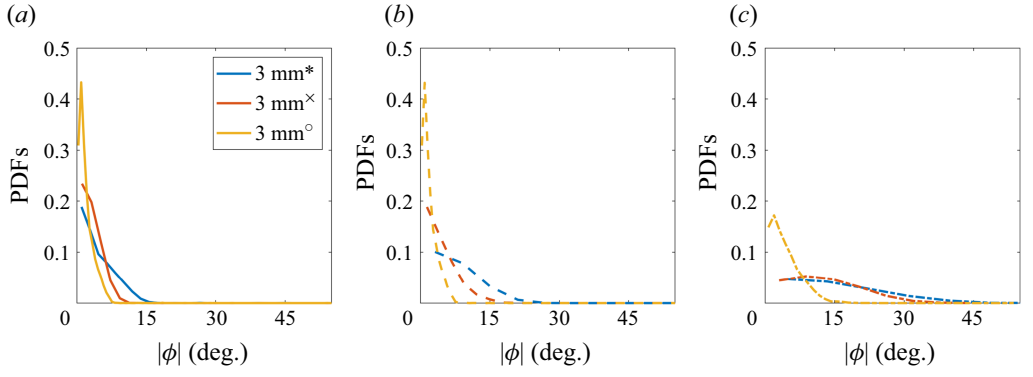

Figure 9. Distributions of two-dimensional projected trajectory angles off the vertical, $|\phi|$, plotted for each disk type in (*a*) quiescent air, (*b*) weaker turbulence and (*c*) stronger turbulence. Colours correspond to those assigned by disk type as in figure 8.

3.3. *Trajectory angles and lateral motions*

We focus here on the turbulence effects on the disk drag in a broad perspective by quantifying how much the disks move laterally under a variety of falling styles. The underlying mechanisms include the rotational-induced lift discussed in Tinklenberg *et al.* (2023) and the cross-flow-induced drag effect discussed in Bagheri & Bonadonna (2016) and Tinklenberg *et al.* (2024). The trajectory angle ϕ within the Particle Tracking Velocimetry observation plane, as defined in figure 3(*b*), is chosen as the key metric for disk lateral dispersion. The average ϕ values are plotted in figure 8 for each flow condition, while the corresponding PDFs are included in figure 9. The stabilising effect of permeability is first observed in quiescent flow, with the solid disk exhibiting the largest angles, and the single hole disks falling more vertically. Overall, turbulence enhances the lateral dispersion of the disks, with the 3 mm$^\times$ following a similar trend in the mean as the 3 mm*. The 3 mm° disks, on the other hand, appear to be swept laterally much less by turbulence, especially under the strong forcing.

This behaviour is likely due to multiple concurring factors. Firstly, the single hole allows for greater permeability of the flow through the single perforation as compared with the smaller perforations of the four quadrant geometry. This is despite the same open area

ratio between the two perforated geometries, suggesting that the single parameter of A_R cannot fully encapsulate the overall dynamics of perforated plates (this may contribute to the settling velocity variability of snow dendrites). Secondly, the larger density of the 3 mm° results in greater rotational inertia I and thus increased I^* for the same nominal area, also leading to increased stabilisation of rotational motions. A disk which is tumbling less and more horizontally oriented is, in fact, reducing the exposed area to horizontal turbulent gusts, thus limiting the lateral motion of the disk. Hence, rotationally stabilised disks are expected to experience less cross-flow-induced drag and fall more vertically in turbulent flows. We infer that competing mechanisms contribute to explain the reduced C_D of the perforated disks: more stably falling, perforated disks offer a larger frontal area to the settling motion and experience a reduced lateral dispersion, while solid disks are more inclined to tumble, which reduces the projected area and makes them more susceptible to lateral wind gusts. With increasing turbulence, the drag coefficient increases, suggesting that cross-flow-induced drag becomes dominant. In fact, the 3 mm* and 3 mm× disks under strong turbulence have a similar C_D and distribution of ϕ. It remains to be understood what controls the disks'tumbling rate and what are the specific roles played by turbulence, moment of inertia and perforation geometry.

3.4. *Falling styles and rotation rates*

The method adopted in Tinklenberg *et al.* (2023, 2024) to determine falling style was based on the angular excursion along the trajectory (Δp_y), and as such relied on having long enough trajectories captured within the field of view to detect an entire 360° rotation for tumbling disks. Due to the faster descent of the thicker 3 mm disks of current focus, less instantaneous frames are captured along a single trajectory. Hence, there is a strong likelihood that even if a disk is tumbling, the entire 360° progression will not be sampled. This will cause an under-detection of tumbling trajectories, biasing the sample towards fluttering and oscillating disk motions. Using the instantaneous values of p_y, the sign change is sufficient to detect the overturning of a disk, indicating tumbling. Comparatively, a fluttering disk will have oscillating values of p_y, but the sign will not change. This method is applied to the disks of focus in this work to obtain falling style percentages shown in figure 10. The 1 mm and 2 mm disks tumble naturally in the quiescent case. Their tumbling is slightly hindered under weak turbulence, and more significantly in the stronger turbulence case. This is due to intermittent air gusts disrupting the regular rotation and the wake shedding, leading to more intense fluttering. The 3 mm and 3 mm* disks see the opposite effect, where the tumbling is enhanced by the turbulence. The different behaviour between the 1 and 2 mm disks and the 3 and 3 mm* disks is due to the different range of Ga and I^*. The 3 mm disks tumble more intermittently in quiescent air, and the turbulence enhances the existing instabilities, causing tumbling to occur more frequently for otherwise fluttering or stable falling disks. As the perforations significantly stabilise the 3 mm× and 3 mm°, the turbulence has a minimal effect on the falling style in these cases, with more persistent fluttering as opposed to tumbling.

For solid disks, it has been shown that the angular velocity and falling style are correlated (Tinklenberg *et al.* 2023). The presence of a strongly bimodal distribution of the trajectory-averaged angular velocity ω_t in the case of the 3 mm* shown in figure 11(a) confirms previous results, with the fluttering mode characterised by a lower ω_t. This, however, is no longer the case for either of the perforated geometries. Despite a residual bimodality for the 3 mm°, figure 11(b, c) show that the angular velocity for the tumbling solid disks, with a peak above 200 rad s^{-1} is significantly reduced by the perforation. We utilise the identification methods used for figure 11 to quantify the conditional tumbling

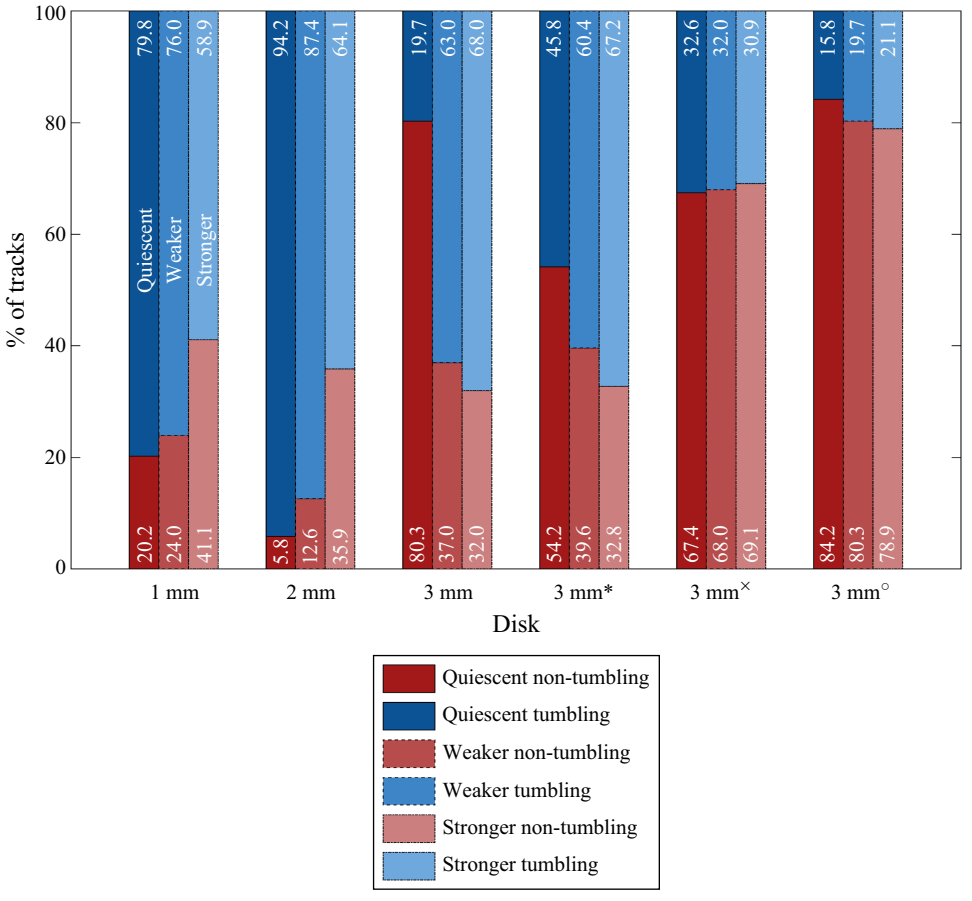

Figure 10. Histograms of trajectory falling style percentages, separated by disk size. Red bars represent non-tumbling and blue represents tumbling. Dark to light shading indicates flow conditions going from quiescent air, to weaker turbulence and stronger turbulence, respectively. Percentage values are listed in white text for both the non-tumbling and tumbling populations on their respective bars.

and non-tumbling angular velocities averages, yielding figure 12. The distinct bimodality of the solid geometries is clear in this view. The near halving of the peak angular velocity measured for tumbling 3mm$^{\times}$ and 3mm$^{\circ}$ disks provides direct evidence of the combined stabilising effect of the perforation, reducing the rotational inertia, and of the permeability stabilising the wake, in both quiescent and turbulent air.

Overall, turbulence has a stronger impact on the angular velocities of non-tumbling particles, while tumbling particles possess sufficient angular momentum to maintain their rotational motion. The 3 mm* disks are somewhat of a transition point between the distinct separation of tumbling versus non-tumbling for the thinner 1 mm, 2 mm and 3 mm disks, and the more stable perforated geometries. Fluttering of the 3 mm* disks becomes less distinguishable from the tumbling as the turbulence is strengthened, resulting in amplified oscillations without always reaching a full rotation. Indeed, according to the classification by Lau *et al.* (2018), the 3 mm* disks fall in the bistable region of the parameter space where steady falling and tumbling coexist.

In order to better quantify the stabilising effects of disk perforation, which are marginally reducing drag and more significantly reducing the angular velocity as compared with the solid disks, we estimate the rotational Strouhal number $Str = fD/V_t$.

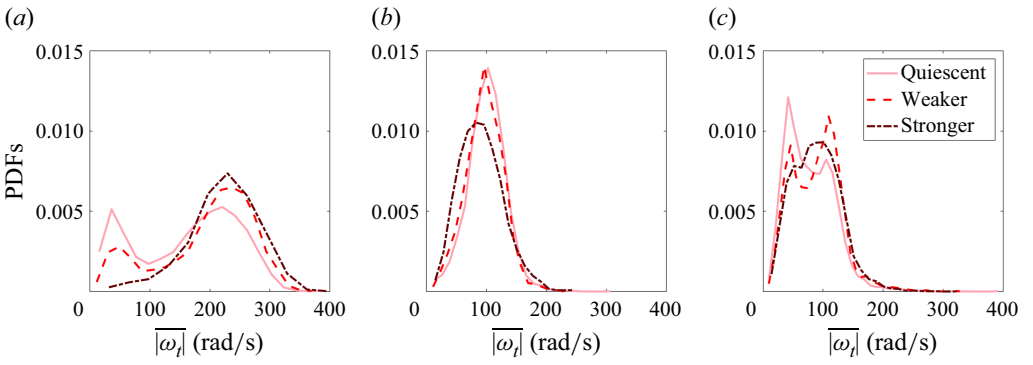

Figure 11. Trajectory-averaged angular velocity distributions for all flow conditions for the (*a*) 3 mm*, (*b*) 3 mm× and (*c*) 3 mm° disks.

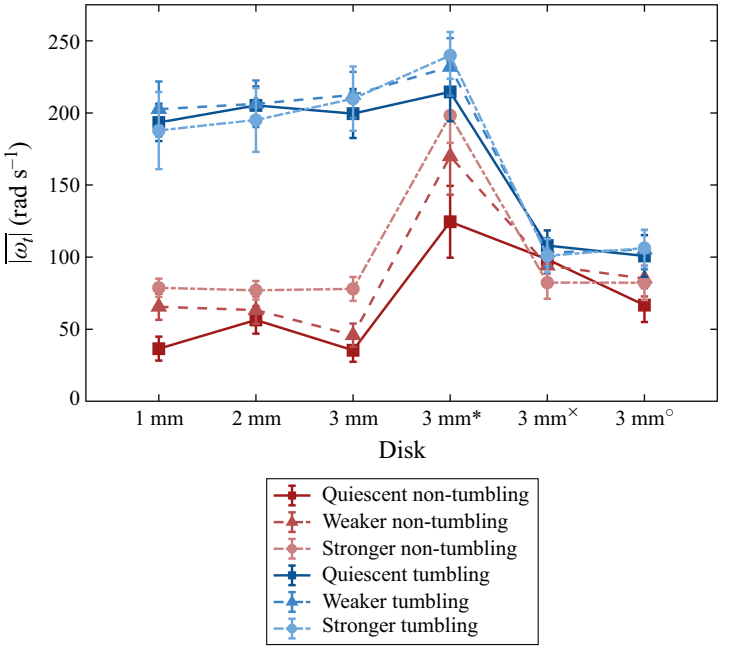

Figure 12. Median angular velocities separated by falling style, where red lines represent non-tumbling disk populations for each disk size and blue lines represent tumbling.

Here, this is based on the peak frequency of the velocity signal, corresponding to twice the frequency of a full tumbling motion ($f = \omega_p/\pi$, with ω_p representing the mode of the ω_t distribution). The Strouhal number is plotted as a function of the inertia ratio in figure 13. As the terminal velocities of the perforated disks are comparable to their solid equivalent, the dampened angular velocity contributes to reduce Str by $\sim 50\,\%$. This results in a deviation from the relation $Str \sim I^{*-0.5}$, which was proposed by Fernandes *et al.* (2007) and observed to fit well to our solid disks. Surprisingly, the 3mm× disks, which most closely resemble snow crystals, exhibit a much stronger deviation, as compared with the single hole disks, which are predominantly stabilised by their density, mass and moment of inertia. This again means that disks with comparable area ratio A_R may still manifest very distinct settling kinematics that are not fully described by the inertia ratio I^*, even

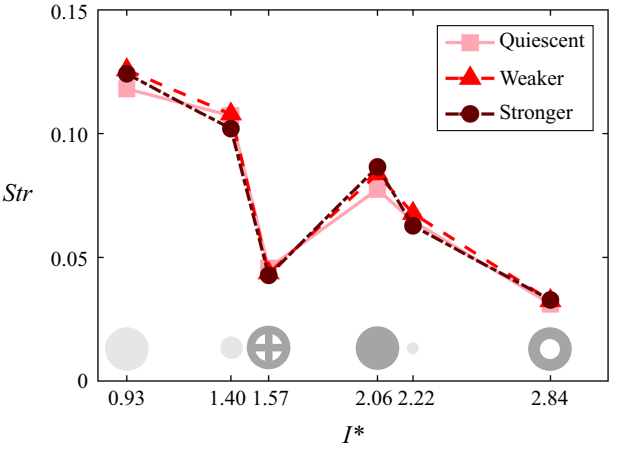

Figure 13. Strouhal number Str plotted as a function of I^*, with respective disk geometry shown along the abscissa. Light coloured disks represent those with $h = 50$ μm and darker represent $h \approx 100$ μm.

when the perforation is included in the estimate of the disk moment of inertia. This suggests that turbulence plays a significant role in the bistable regime, but with a more marginal effect when the disk falling style is well defined by the material properties and I^*. The perforation geometry, however, when associated with a different permeability and regardless of A_R, manifests a significant effect in the dampening of ω_t and in the deviation from the $Str - I^*$ dependency.

4. Discussion

The parameter space to study the coupled settling and rotational kinematics of snow plates and dendrites is multidimensional and expected to include the additional effects of the ambient flow. Figure 14 is inspired by the early work of Kajikawa & Okuhara (1997), where a limited number of more or less rimed snow plates have been mapped in the inertia ratio (I^*) and Reynolds number (Re) phase space. In their original contribution, the authors investigated how increased riming, affecting the particle density and aspect ratio, leads to different falling style, classified as (i) rotation or spiral (R-S), affine to our tumbling definition and quantification, and (ii) swing or non-rotation (S-N), which includes fluttering and flat falling. As opposed to the predictable Galileo number, which is based on the gravitational velocity U_g, $Re = V_t D/\nu$ features the actual average settling velocity and thus incorporates the correct particle drag and turbulence effects. Our solid (D $\geqslant$ 1 mm) and perforated disks in figure 14 are coloured based on the observed tumbling percentage, and can thus be compared with the R-S classification. Laboratory and field data exhibit fairly consistent settling kinematics and, to a lesser extent, tumbling characteristics in a range of $100 < Re < 500$ and $I^* > 0.7$. With increasing mass (along with terminal velocity, and Re) and permeability, the disks are more rotationally stable, while with increasing ambient turbulence and drag, disks are more keen to tumble. Based on this scattered laboratory and field data, we cannot develop a predictive model, but only speculate about natural conditions favouring snow particle tumbling. Thin and light disks are likely to feel small eddies in turbulent air flows and develop a wake able to sustain autorotation, providing they are large or dense enough to reach $Re > 100$. Natural candidates in such a phase space are relatively large, unrimed plates, and to a lesser extent, snow dendrites, which may, however, be stabilised by their own permeability.

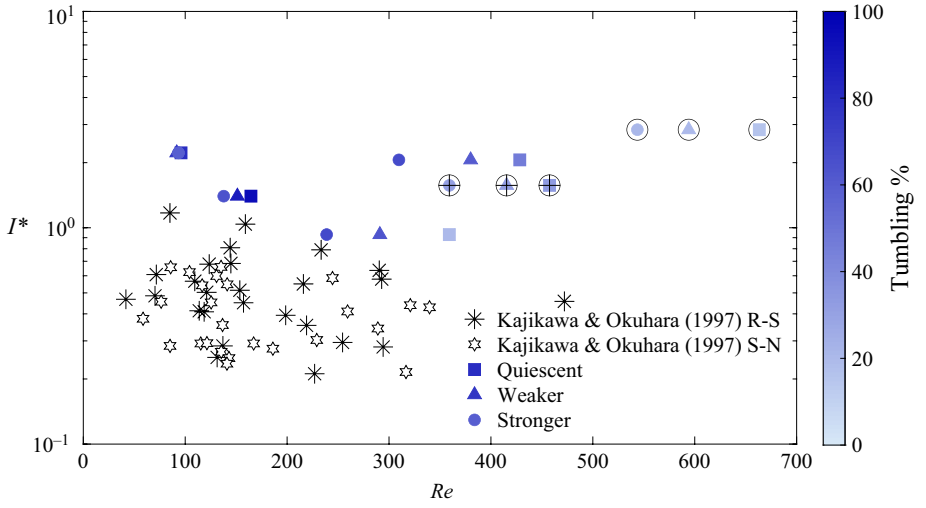

Figure 14. Inertia ratio I^* and Reynolds number Re scatter plot of currently investigated solid and perforated disks under the three forcing regimes. The symbol colour coding is set to quantify the tumbling percentage of the disk as indicated in the histograms of figure 10. The perforated disks 3mm$^\times$ and 3mm$^\circ$ are highlighted by $\oplus$ and $\bigcirc$ overlapped symbols. Our results are overlapped with field data of more or less rimed plates and dendrites as classified by Kajikawa (1992) into R-S (spiral or rotation) and S-N (swing and non-rotation).

The snow dendrite and plate density (Locatelli & Hobbs 1974; Li *et al.* 2023) is somewhat smaller than the solid disks tested here, and their typical size, ranging from 0.1 to 1 mm, is only partially overlapping with our disks in a range where tumbling quantification is challenging even at laboratory scale (Tinklenberg *et al.* 2024). Results from McCorquodale & Westbrook (2021*b*) with snow analogues in quiescent liquids reproduce the range of Re, but are limited to a low range of I^* up to 0.01. It thus appears that the phase space $0.2 < I^* < 0.7$ and $50 < Re < 300$ is meteorologically relevant and worth exploring statistically in future experiments. Transition between regimes may occur around $Re \simeq 100$ and $I^* \simeq 0.5$, bordering the chaotic regime as suggested by Field *et al.* (1997) and Jayaweera & Mason (1965), which may explain the overlap between rotational (R-S) and swing/flat (S-N) crystals falling in Kajikawa & Okuhara (1997). In addition, with different levels of turbulent forcing in the above regimes, the associated marginal stability curves may need to be redefined, which again emphasises the importance of controlled laboratory experiments with correct particle shapes, fluid density ratios and a range of quiescent to turbulent forcing conditions. Finally, we stress that the observed scatter in figure 14, can be interpreted in view of the Str and I^* deviation exhibited by the 3mm$^\times$ disks in figure 13 and the 3 mm disks in figure 10. Accordingly, when the disk falling style is in a bistable transitioning regime, turbulence intensity has a significant effect; however, when the disks are tumbling, the permeability, rather than the size of the perforation or the turbulence, plays a key role. Since turbulence and permeability are not explicitly accounted for, both the tumbling frequencies in figure 14 and the drag coefficients in figure 5 exhibit significant variability that propagates to the settling velocity.

5. Conclusion

We have reported on an experimental study of thin, mm-sized solid and perforated disks falling in air. The considered range of non-dimensional parameters, $\chi = 5 - 60$, $Re = 10 - 663$ and $I^* \approx O(1)$, is relevant to the settling of snow plate crystals and dendrites in

the atmosphere. Still, to our knowledge, it has only been recently investigated in laboratory experiments by Tinklenberg *et al.* (2024). Therein, we did not attempt to broadly scan the parameter space, but rather expanded the number of realisations for each considered case in order to achieve the statistical description of a settling process characterised by coexisting falling styles and high variability, even in quiescent flows (Lau *et al.* 2018; Tinklenberg *et al.* 2023). The dynamics of solid disks is compared here with those with perforated geometries in both quiescent air and in two homogeneous turbulence flows with different Re_λ. Two types of perforated disks, characterised by four quadrant and single hole geometries with matching area ratios and solidity, were investigated to assess the specific influence of the perforation shape and size on the settling kinematics, as well as the predictive ability of currently available models to estimate the terminal velocity V_t. Using laser illumination and high-speed imaging, we have gathered and analysed the objects translational and rotational kinematics based on thousands of trajectories obtained in repeated runs with volumetric concentration of $O(10^{-6})$ comparable to natural snowfalls (Li *et al.* 2021*a*).

The main results of our investigation can be summarised as follows:

(i) When $Re \geqslant 100$, turbulence consistently reduces the fall speed of perforated disks, as compared with quiescent flow results, confirming the results of Tinklenberg *et al.* (2024) on solid disks and supporting the statistical predominance of cross-flow-induced drag enhancement over preferential sweeping in all the conditions investigated.

(ii) Perforated disks are stabilised in their descent motion, and therefore tumble less frequently and at a reduced angular velocity. This result is robust in both quiescent air and homogeneous turbulence. For the solid disk, we see a strongly bimodal distribution of the angular velocity, which directly correlates with the falling style of the disks. For example, the peak tumbling angular velocity for the solid disks is reduced by 50 % for the perforated geometries, even when comparing disks with the same diameter and thicknesses (3mm$^\times$ perforated disk versus the solid 3mm*). However, different perforation geometries lead to specific reductions in the Strouhal number, as highlighted by observed deviations from the functional dependency on the rotational inertial properties, I^*, characteristic of solid disks (figure 13). This points again at the key role of permeability, rather than the area ratio or turbulence, in settling the tumbling dynamics of perforated disks in the conditions investigated.

(iii) The area ratio A_R is an important parameter in determining the fall speed, and needs to be appropriately taken into account in settling velocity models as inspired by Böhm (1989). However, A_R cannot entirely describe the disk drag and settling dynamics. This is because the disk permeability may vary for the same A_R and the associated rotational effects may contribute to the observed differences in the $C_D(Re)$ curves in figure 5 and in the average settling velocity.

(iv) Heymsfield & Westbrook (2010) reasonably reproduces the fall speed of model hydrometeors in quiescent air, although it shows a systematic under-prediction. The latter is even more marked in Böhm (1989) and Mitchell (1996), which mostly rely on laboratory experiments in liquids. In this respect, previous laboratory studies of Re-analogous plate settling in viscous liquids yield a distinctly different C_D plateau, which deviates from the present data at $Re \approx 100$. In the extension to atmospheric precipitation, this again highlights the importance of high-density-ratio experiments under varying turbulence intensities to reproduce the variability in falling styles and tumbling rate of high inertia ratio particles such as snow plates and dendrites.

(v) The good agreement between our results under turbulence and the Heymsfield & Westbrook (2010) model confirms that ambient turbulence, which clearly modulates the field data and impacts their fitting constant, should be explicitly parameterised in hydrometeor fall speed and drag models.

In summary, the disk settling velocity and tumbling behaviour reveal a strong coupling between falling styles, particle inertial properties, turbulence levels and flow permeability. It is inferred that ambient turbulence increases the disk drag coefficient mostly through cross-flow-induced (nonlinear) drag. Perforation effects are partially captured by the area ratio parameterisation of the terminal velocity in Böhm (1989), Heymsfield & Westbrook (2010) and McCorquodale & Westbrook (2021*a*); however, permeability strongly influences the disk tumbling rate, which has a secondary, although non-negligible, effect on the drag coefficient.

An improved definition of the surface porosity and permeability of frozen hydrometeors, or generally falling objects, would be of great interest in a modelling study to develop a more comprehensive understanding of hole placement and the correlation to stabilising wake structures developed. For instance, in the case of fluffy snow flake aggregates, the many small perforations may not only reduce the effective density but perhaps randomise the wake and the associated vortex shedding, with an increased stabilising effect. Other applications in literature with similar implications include the flight of dandelions (Cummins *et al.* 2018; Qiu *et al.* 2020), leakiness of bristled insect wings (Ford *et al.* 2019; Lee *et al.* 2020; O'Callaghan & Lehmann 2023) and pipe flow through a perforated plate or screen (Bayazit *et al.* 2014).

The effects of turbulence and permeability could potentially be decoupled when the disk falling style is robustly predicted. Unfortunately, when disks lay in the bistable $I^* - Ga$ (or $I^* - Re$) phase space, all the above variables are intertwined, settling velocity prediction remains very challenging, and large variability is expected in the field measurements. This is amplified when a range of snow morphologies and sizes characterise the same snowfall event, as observed by Li *et al.* (2023, 2024). The variability in snow morphology may lead to the simultaneous occurrence of various particle–turbulence interaction mechanisms, featuring e.g. graupel-like particles experiencing preferential sweeping, clustering and settling velocity enhancement (Nemes *et al.* 2017; Li *et al.* 2021*a*,*b*), along with plate-like crystals affected by loitering, cross-flow-induced drag and settling velocity reduction (Garrett & Yuter 2014; Singh *et al.* 2023). We thus infer that the thick tails, skewness and other non-Gaussian features observed in settling velocity distributions from field data may be caused not only by a range in size and snow morphologies, but also by the different effects that turbulence exerts on specific subsets of particles according to various interaction mechanisms.

Funding. This work was supported by the US National Science Foundation (Physical and Dynamic Meteorology program) through grant NSF-AGS-1822192 and by the National Aeronautics and Space Administration (Weather and Atmospheric Dynamics program) through grant 80NSSC20K0912.

Declaration of interests. The authors report no conflict of interest.

References

Abraham, F.F. 1970 Functional dependence of drag coefficient of a sphere on Reynold snumber. *Phys. Fluids* **13** (8), 2194–2195.

Aliseda, A., Cartellier, A., Hainaux, F. & Lasheras, J.C. 2002 Effect of preferential concentration on the settling velocity of heavy particles in homogeneous isotropic turbulence. *J. Fluid Mech.* **468**, 77–105.

Auer, A.H. & Veal, D.L. 1970 The dimension of ice crystals in natural clouds. *J. Atmos. Sci.* **27** (6), 919–926.

AUGUSTE, F., MAGNAUDET, J. & FABRE, D. 2013 Falling styles of disks. *J. Fluid Mech.* **719**, 388–405.
BAGHERI, G. & BONADONNA, C. 2016 On the drag of freely falling non-spherical particles. *Powder Technol.* **301**, 526–544.
BAKER, L.J. & COLETTI, F. 2022 Experimental investigation of inertial fibres and disks in a turbulent boundary layer. *J. Fluid Mech.* **943**, A27.
BAYAZIT, Y., SPARROW, E.M. & JOSEPH, D.D. 2014 Perforated plates for fluid management: plate geometry effects and flow regimes. *Intl J. Therm. Sci.* **85**, 104–111.
BERK, T. & COLETTI, F. 2021 Dynamics of small heavy particles in homogeneous turbulence: a Lagrangian experimental study. *J. Fluid Mech.* **917**, A47.
BHOWMICK, T., SEESING, J., GUSTAVSSON, K., GUETTLER, J., WANG, Y., PUMIR, A., MEHLIG, B. & BAGHERI, G. 2024 Inertia induces strong orientation fluctuations of nonspherical atmospheric particles. *Phys. Rev. Lett.* **132** (3), 034101.
BRANDES, E.A., IKEDA, K., THOMPSON, G. & SCHÖNHUBER, M. 2008 Aggregate terminal velocity/temperature relations. *J. Appl. Meteorol. Clim.* **47** (10), 2729–2736.
BRANDT, L. & COLETTI, F. 2022 Particle-laden turbulence: progress and perspectives. *Annu. Rev. Fluid Mech.* **54** (1), 159–189.
BRÉON, F.-M. & DUBRULLE, B. 2004 Horizontally oriented plates in clouds. *J. Atmos. Sci.* **61** (23), 2888–2898.
BYRON, M., EINARSSON, J., GUSTAVSSON, K., VOTH, G., MEHLIG, B. & VARIANO, E. 2015 Shape-dependence of particle rotation in isotropic turbulence. *Phys. Fluids* **27** (3), 035101.
BÖHM, H.P. 1989 A general equation for the terminal fall speed of solid hydrometeors. *J. Atmos. Sci.* **46** (15), 2419–2427.
BÖHM, J.P. 1992 A general hydrodynamic theory for mixed-phase microphysics. Part I: drag and fall speed of hydrometeors. *Atmos. Res.* **27** (4), 253–274.
CARTER, D.W. & COLETTI, F. 2017 Scale-to-scale anisotropy in homogeneous turbulence. *J. Fluid Mech.* **827**, 250–284.
CARTER, D.W. & COLETTI, F. 2018 Small-scale structure and energy transfer in homogeneous turbulence. *J. Fluid Mech.* **854**, 505–543.
CARTER, D., PETERSEN, A., AMILI, O. & COLETTI, F. 2016 Generating and controlling homogeneous air turbulence using random jet arrays. *Exp. Fluids* **57** (12), 189.
CHRUST, M., BOUCHET, G. & DUŠEK, J. 2013 Numerical simulation of the dynamics of freely falling discs. *Phys. Fluids* **25** (4), 044102.
CUMMINS, C., SEALE, M., MACENTE, A., CERTINI, D., MASTROPAOLO, E., VIOLA, I.M. & NAKAYAMA, N. 2018 A separated vortex ring underlies the flight of the dandelion. *Nature* **562** (7727), 414–418.
FERNANDES, P.C., RISSO, F., ERN, P. & MAGNAUDET, J. 2007 Oscillatory motion and wake instability of freely rising axisymmetric bodies. *J. Fluid Mech.* **573**, 479–502.
FERRANTE, A. & ELGHOBASHI, S. 2003 On the physical mechanisms of two-way coupling in particle-laden isotropic turbulence. *Phys. Fluids* **15** (2), 315–329.
FIELD, S.B., KLAUS, M., MOORE, M.G. & NORI, F. 1997 Chaotic dynamics of falling disks. *Nature* **388** (6639), 252–254.
FORD, M.P., KASOJU, V.T., GADDAM, M.G. & SANTHANAKRISHNAN, A. 2019 Aerodynamic effects of varying solid surface area of bristled wings performing clap and fling. *Bioinspir. Biomim* **14** (4), 046003.
FORNARI, W., PICANO, F. & BRANDT, L. 2016*a* Sedimentation of finite-size spheres in quiescent and turbulent environments. *J. Fluid Mech.* **788**, 640–669.
FORNARI, W., PICANO, F., SARDINA, G. & BRANDT, L. 2016*b* Reduced particle settling speed in turbulence. *J. Fluid Mech.* **808**, 153–167.
GARRETT, T.J., FALLGATTER, C., SHKURKO, K. & HOWLETT, D. 2012 Fall speed measurement and high-resolution multi-angle photography of hydrometeors in free fall. *Atmos. Meas. Tech.* **5** (11), 2625–2633.
GARRETT, T.J. & YUTER, S.E. 2014 Observed influence of riming, temperature, and turbulence on the fallspeed of solid precipitation. *Geophys. Res. Lett.* **41** (18), 6515–6522.
GOOD, G.H., IRELAND, P.J., BEWLEY, G.P., BODENSCHATZ, E., COLLINS, L.R. & WARHAFT, Z. 2014 Settling regimes of inertial particles in isotropic turbulence. *J. Fluid Mech.* **759**, R3.
GRABOWSKI, W.W. & WANG, L.-P. 2013 Growth of cloud droplets in a turbulent environment. *Annu. Rev. Fluid Mech.* **45** (1), 293–324.
HASSAINI, R. & COLETTI, F. 2022 Scale-to-scale turbulence modification by small settling particles. *J. Fluid Mech.* **949**, A30.
HASSAINI, R., PETERSEN, A.J. & COLETTI, F. 2023 Effect of two-way coupling on clustering and settling of heavy particles in homogeneous turbulence. *J. Fluid Mech.* **976**, A12.

HEYMSFIELD, A.J. & WESTBROOK, C.D. 2010 Advances in the estimation of ice particle fall speeds using laboratory and field measurements. *J. Atmos. Sci.* **67** (8), 2469–2482.
JAYAWEERA, K.O.L.F. & COTTIS, R.E. 1969 Fall velocities of plate-like and columnar ice crystals. *Q. J. R. Meteorol. Soc.* **95** (406), 703–709.
JAYAWEERA, K.O.L.F. & MASON, B.J. 1965 The behaviour of freely falling cylinders and cones in a viscous fluid. *J. Fluid Mech.* **22** (04), 709.
JEFFERY, G.B. 1922 The motion of ellipsoidal particles immersed in a viscous fluid. *Proc. R. Soc. Lond. A* **102** (715), 161–179.
KAJIKAWA, M. 1992 Observations of the falling motion of plate-like snow crystals part I: the free-fall patterns and velocity. *J. Met. Soc. Japan II* **70** (1), 1–9.
KAJIKAWA, M. & OKUHARA, K. 1997 Observations of the falling motion of plate-like snow crystals. *J. Met. Soc. Japan II* **75** (4), 811–818.
KHVOROSTYANOV, V.I. & CURRY, J.A. 2002 Terminal velocities of droplets and crystals: power laws with continuous parameters over the size spectrum. *J. Atmos. Sci.* **59** (11), 1872–1884.
KHVOROSTYANOV, V.I. & CURRY, J.A. 2005 Fall velocities of hydrometeors in the atmosphere: refinements to a continuous analytical power law. *J. Atmos. Sci.* **62** (12), 4343–4357.
LAU, E.M., HUANG, W.-X. & XU, C.-X. 2018 Progression of heavy plates from stable falling to tumbling flight. *J. Fluid Mech.* **850**, 1009–1031.
LEE, M., LEE, S.H. & KIM, D. 2020 Stabilized motion of a freely falling bristled disk. *Phys. Fluids* **32** (11), 113604.
LI, C., LIM, K., BERK, T., ABRAHAM, A., HEISEL, M., GUALA, M., COLETTI, F. & HONG, J. 2021*a* Settling and clustering of snow particles in atmospheric turbulence. *J. Fluid Mech.* **912**, A49.
LI, J., ABRAHAM, A., GUALA, M. & HONG, J. 2021*b* Evidence of preferential sweeping during snow settling in atmospheric turbulence. *J. Fluid Mech.* **928**, A8.
LI, J., GUALA, M. & HONG, J. 2023 Snow particle analyzer for simultaneous measurements of snow density and morphology. *J. Geophys. Res.: Atmospheres* **128** (16), e2023JD038987.
LI, J., GUALA, M. & HONG, J. 2024 Field investigation of 3D snow settling dynamics under weak atmospheric turbulence. *J. Fluid Mech.* **997**, A33.
LIST, R. & SCHEMENAUER, R.S. 1971 Free-fall behavior of planar snow crystals, conical graupel and small hail. *J. Atmos. Sci.* **28** (1), 110–115.
LOCATELLI, J.D. & HOBBS, P.V. 1974 Fall speeds and masses of solid precipitation particles. *J. Geophys. Res.* **79** (15), 2185–2197.
MAGONO, C. & LEE, C.W. 1966 Meteorological Classification of Natural Snow Crystals. *J. Faculty Sci.* **2**, 321–335.
MATROSOV, S.Y., REINKING, R.F., KROPFLI, R.A., MARTNER, B.E. & BARTRAM, B.W. 2001 On the use of radar depolarization ratios for estimating shapes of ice hydrometeors in winter clouds. *J. Appl. Meteorol.* **40** (3), 479–490.
MCCORQUODALE, M.W. & WESTBROOK, C.D. 2021*a* TRAIL: a novel approach for studying the aerodynamics of ice particles. *Q. J. R. Meteorol. Soc.* **147** (734), 589–604.
MCCORQUODALE, M.W. & WESTBROOK, C.D. 2021*b* TRAIL part 2: a comprehensive assessment of ice particle fall speed parametrisations. *Q. J. R. Meteorol. Soc.* **147** (734), 605–626.
MITCHELL, D.L. 1996 Use of mass- and area-dimensional power laws for determining precipitation particle terminal velocities. *J. Atmos. Sci.* **53** (12), 1710–1723.
MITCHELL, D.L. & HEYMSFIELD, A.J. 2005 Refinements in the treatment of ice particle terminal velocities, highlighting aggregates. *J. Atmos. Sci.* **62** (5), 1637–1644.
MORICHE, M., HETTMANN, D., GARCÍA-VILLALBA, M. & UHLMANN, M. 2023 On the clustering of low-aspect-ratio oblate spheroids settling in ambient fluid. *J. Fluid Mech.* **963**, A1.
MORICHE, M., UHLMANN, M. & DUŠEK, J. 2021 A single oblate spheroid settling in unbounded ambient fluid: a benchmark for simulations in steady and unsteady wake regimes. *Intl J. Multiphase Flow* **136**, 103519.
NEMES, A., DASARI, T., HONG, J., GUALA, M. & COLETTI, F. 2017 Snowflakes in the atmospheric surface layer: observation of particle–turbulence dynamics. *J. Fluid Mech.* **814**, 592–613.
NOEL, V. & CHEPFER, H. 2004 Study of ice crystal orientation in cirrus clouds based on satellite polarized radiance measurements. *J. Atmos. Sci.* **61** (16), 2073–2081.
O'CALLAGHAN, F. & LEHMANN, F.-O. 2023 Flow development and leading edge vorticity in bristled insect wings. *J. Compar. Physiol. A* **209** (2), 219–229.
PETERSEN, A.J., BAKER, L. & COLETTI, F. 2019 Experimental study of inertial particles clustering and settling in homogeneous turbulence. *J. Fluid Mech.* **864**, 925–970.

QIU, F.-S., HE, T.-B. & BAO, W.-Y. 2020 Effect of porosity on separated vortex rings of dandelion seeds. *Phys. Fluids* **32** (11), 113104.
ROHATGI, A. 2021 WebPlotDigitizer.
SASSEN, K. 1980 Remote sensing of planar ice crystal fall attitudes. *J. Met. Soc. Japan II* **58** (5), 422–429.
SHAW, R.A. 2003 Particle-turbulence interactions in atmospheric clouds. *Annu. Rev. Fluid Mech.* **35** (1), 183–227.
SINGH, D.K., PARDYJAK, E.R. & GARRETT, T.J. 2023 A universal scaling law for Lagrangian snowflake accelerations in atmospheric turbulence. *Phys. Fluids* **35** (12), 123336.
STOUT, J.R., WESTBROOK, C.D., STEIN, T.H.M. & MCCORQUODALE, M.W. 2024 Stable and unstable fall motions of plate-like ice crystal analogues. *Atmos. Chem. Phys.* **24** (19), 11133–11155.
SÁNCHEZ-RODRÍGUEZ, J. & GALLAIRE, F. 2025 Tumbling elimination induced by permeability: an experimental approach. *Phys. Rev. Fluids* **10**, 013904.
TINKLENBERG, A., GUALA, M. & COLETTI, F. 2023 Thin disks falling in air. *J. Fluid Mech.* **962**, A3.
TINKLENBERG, A., GUALA, M. & COLETTI, F. 2024 Turbulence effect on disk settling dynamics. *J. Fluid Mech.* **992**, A3.
VAGNOLI, G., ZAMPOGNA, G.A., CAMARRI, S., GALLAIRE, F. & LEDDA, P.G. 2023 Permeability sets the linear path instability of buoyancy-driven disks. *J. Fluid Mech.* **955**, A29.
VARIANO, E.A. & COWEN, E.A. 2008 A random-jet-stirred turbulence tank. *J. Fluid Mech.* **604**, 1–32.
VINCENT, L., SHAMBAUGH, W.S. & KANSO, E. 2016 Holes stabilize freely falling coins. *J. Fluid Mech.* **801**, 250–259.
VOTH, G.A. & SOLDATI, A. 2017 Anisotropic particles in turbulence. *Annu. Rev. Fluid Mech.* **49** (1), 249–276.
VÁZQUEZ-MARTÍN, S., KUHN, T. & ELIASSON, S. 2021 Shape dependence of snow crystal fall speed. *Atmos. Chem. Phys.* **21** (10), 7545–7565.
WANG, L.-P. & MAXEY, M.R. 1993 Settling velocity and concentration distribution of heavy particles in homogeneous isotropic turbulence. *J. Fluid Mech.* **256**, 27–68.
WANG, P.K. 2021 Observational studies of ice hydrometeors and their fall behavior. In *Motions of Ice Hydrometeors in the Atmosphere: Numerical Studies and Implications*. Springer.
WESTBROOK, C.D. & SEPHTON, E.K. 2017 Using 3-D-printed analogues to investigate the fall speeds and orientations of complex ice particles. *Geophys. Res. Lett.* **44** (15), 7994–8001.
WILLMARTH, W.W., HAWK, N.E. & HARVEY, R.L. 1964 Steady and unsteady motions and wakes of freely falling disks. *Phys. Fluids* **7** (2), 197–208.
ZHANG, W., BI, D. & WEI, Y. 2023 Falling styles of perforated disks. *Intl J. Multiphase Flow* **161**, 104401.